



Metabolome and Proteome Profiling of Complex I Deficiency Induced by Rotenone

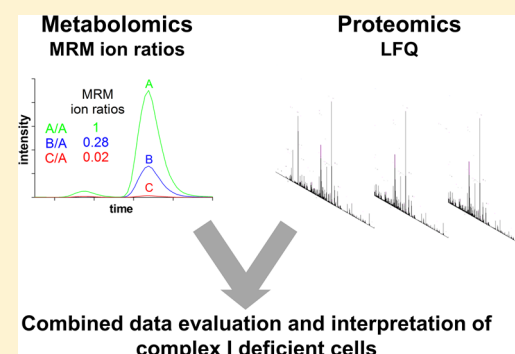
Ina Gielisch[†] and David Meierhofer*

Max Planck Institute for Molecular Genetics, Ihnestraße 63-73, 14195 Berlin, Germany

S Supporting Information

ABSTRACT: Complex I (CI; NADH dehydrogenase) deficiency causes mitochondrial diseases, including Leigh syndrome. A variety of clinical symptoms of CI deficiency are known, including neurodegeneration. Here, we report an integrative study combining liquid chromatography–mass spectrometry (LC–MS)-based metabolome and proteome profiling in CI deficient HeLa cells. We report a rapid LC–MS-based method for the relative quantification of targeted metabolome profiling with an additional layer of confidence by applying multiple reaction monitoring (MRM) ion ratios for further identity confirmation and robustness. The proteome was analyzed by label-free quantification (LFQ). More than 6000 protein groups were identified. Pathway and network analyses revealed that the respiratory chain was highly deregulated, with metabolites such as FMN, FAD, NAD⁺, and ADP, direct players of the OXPHOS system, and metabolites of the TCA cycle decreased up to 100-fold. Synthesis of functional iron–sulfur clusters, which are of central importance for the electron transfer chain, and degradation products like bilirubin were also significantly reduced. Glutathione metabolism on the pathway level, as well as individual metabolite components such as NADPH, glutathione (GSH), and oxidized glutathione (GSSG), was downregulated. Overall, metabolome and proteome profiles in CI deficient cells correlated well, supporting our integrated approach.

KEYWORDS: Complex I deficiency (CI), multiple reaction monitoring (MRM), iron sulfur cluster, mass spectrometry, metabolome profiling, network analysis, pathway analysis, proteome profiling, rotenone



INTRODUCTION

Complex I (NADH dehydrogenase, CI) is part of the mitochondrial oxidative phosphorylation (OXPHOS) system and plays critical roles in transferring electrons and pumping protons to maintain the electrochemical gradient across the inner mitochondrial membrane. This gradient is used by the mitochondrial ATPase to synthesize ATP, the main source of ATP under aerobic conditions in eukaryotes. The cause of CI deficiency can originate from both mitochondrial or nuclear DNA mutation, as both genomes contribute subunits to CI. CI deficiency is the most frequent mitochondrial disorder, characterized by clinical and genetic heterogeneity,¹ and includes Leber's hereditary optic neuropathy (LHON), mitochondrial encephalomyopathy, lactic acidosis, and stroke-like episodes (MELAS), myoclonic epilepsy with ragged red fibers (MERRF), and Leigh syndrome (LS).

Rotenone is frequently used to study CI dysfunction.^{2–7} It is a specific inhibitor⁸ that binds to the ubiquinone binding site of CI,^{9,10} thus preventing electron transfer via FMN (flavin mononucleotide) to coenzyme Q10. The repercussion of this is the interruption of the entire oxidative phosphorylation chain, simulating the features of CI deficiency.

Metabolome profiling is a complex task because of huge structural diversities, variations of size, and polarities of metabolites. No single analytical method is capable of

comprehensive metabolic profiling¹¹ and hence different column and buffer settings for an optimal LC separation of metabolites are needed. A targeted LC–MS approach,¹² the high-quality analysis of a subset of predefined metabolites with known chemical structures, is thus the ideal method. Once established, the target-based approach is advantageous because of its fast and reliable measurement of the selected analytes in complex samples. MRM has been commonly used for the analysis of small molecules and peptides,¹³ but the identification of metabolites based on one MRM is still error-prone. Previous studies^{14–18} have used only one transition for metabolite identification. To increase the confidence of metabolite identification, some investigators already use three transitions.^{19–21}

The metabolic and proteomic states can reveal information on the genetic, physiological, or functional status of the system. Combining proteome and metabolome approaches can be very useful to obtain deeper and better insight into living systems.

Here, we investigated CI deficiency introduced by rotenone and analyzed the interplay of proteins and metabolites under

Special Issue: Environmental Impact on Health

Received: August 28, 2014

Published: October 31, 2014

well-defined conditions. As an additional layer of confidence in metabolite identification, we employ metabolite-specific transition ratios, MRM ion ratios. This concept was first described in the context of small molecules as the branching ratio, where each time a small molecule was fragmented and multiple product ions were detected the ratio of these ions to one another was consistent.²²

In this study, we quantitatively profiled the entire proteome and selected metabolites to obtain a holistic view of induced CI deficiency. For quantitative proteome profiling, we used a shotgun LC–MS/MS approach and applied a label-free quantification method²³ to compare CI deficiency to controls in biological triplicates. The combination of three MRMs and their MRM ion ratios results in an enhanced method for the reliable, rapid, and quantitative profiling of metabolites. We detected molecular changes in CI deficient cells by quantitatively analyzing shotgun proteomics and targeted metabolomics data, applying bioinformatics network approaches, and we identified several biological pathways and hub proteins that are dysregulated in rotenone-treated HeLa cells.

MATERIALS AND METHODS

Metabolite Tuning and LC–MS/MS Optimization for MRM Ion Ratios

The target metabolites were selected to cover most of the important metabolic pathways in mammals: 273 metabolites in total. Pure metabolites were dissolved to a final concentration of 1 μM in MeOH and 0.1% formic acid, and 10 mM ammonium hydroxide was added and injected by a syringe (7 μL/min) into the triple quadrupole hybrid ion trap mass spectrometer (QTrap 6500, ABSciex, Toronto, Canada). Precursor ions were fragmented in positive and negative electrospray ionization (ESI) modes, and the seven most intense fragment peaks in each polarity were chosen and optimized for the following parameters: declustering potential (DP) for precursor ions, collision energy (CE), and collision cell exit potential (CXP) for fragment ions. Transitions were monitored and acquired at unit resolution (peak width at 50% was 0.7 ± 0.1 Da tolerance) in quadrupole Q1 and Q3. In order to identify the transitions with the highest ion counts and an optimal LC separation of the metabolites, we ran all metabolites on an online-coupled LC–MS/MS system: 1290 Infinity UHPLC (Agilent, Santa Clara, CA, USA), QTrap 6500 (ABSciex, Toronto, Canada). The following columns were used for LC separation of metabolites: a Reprosil-PUR C18-AQ (1.9 μm, 120 Å, 150 × 2 mm ID; Dr. Maisch; Ammerbuch, Germany) column and a zicHILIC (3.5 μm, 100 Å, 150 × 2.1 mm ID; di2chrom; Marl, Germany) column at a controlled temperature of 30 °C. All LC running conditions are described in Supporting Information Table S1 and the LC Conditions for Metabolomics section. Data acquisition was performed with an ion spray voltage of 5.5 kV in positive mode and 4.5 kV in negative mode of the ESI source, N2 as the collision gas was set to high, curtain gas was set to 30 psi, ion source gas 1 and 2 were set to 50 and 70 psi, respectively, and an interface heater temperature of 350 °C was used, which was operated with AB Sciex Analyst 1.6.1 software with components for 6500 series instruments.

The LC method with the best metabolite separation and the three metabolite transitions with the highest ion count (peak area) were picked for the final LC–MRM method. In order to calculate MRM ion ratios, the most intense peak was set to 1, and the two smaller peaks were divided by the most intense peak (all

MRM ion ratios are available in Supporting Information Table S2). Three replicates for each metabolite were used to calculate the final MRM ion ratios, which are used as reference values. The presence of peaks was compared to databases such as Metlin²⁴ and HMDB²⁵ in order to confirm fragment masses. All evaluated metabolites can be found in Supporting Information Table S2. For a few metabolites, we lacked the substance for tuning and therefore solely relied on our own MS/MS spectra from biological samples matching database spectra (the three most intense transitions were taken), or we used only transitions from available database resources, as indicated in Supporting Information Table S2. Therefore, instrument settings for these nontuned metabolites could not be optimized.

Cell Culture

HeLa (human cervical cancer) cells were cultivated in DMEM (Invitrogen, Carlsbad, CA, USA) containing 4.5 g/L glucose supplemented with 10% FBS and 1% penicillin–streptomycin–neomycin antibiotic mixture (Invitrogen, Carlsbad, CA, USA) at 37 °C in a humidified atmosphere of 5% CO₂. The cells were grown in 300 cm² polystyrene flasks to approximately 90% confluence. Fifty milliliters of fresh media supplemented with 1 μM rotenone or DMSO as control was added, and after 38 h of incubation, cells were sampled for proteome and metabolome analyses. The experiment was done in biological triplicates for rotenone-treated and controls.

Measurement of Complex I Enzyme Activity, Cell Viability, and Apoptosis

In order to inhibit complex I enzyme activity efficiently as well as to keep the cells proliferating and to prevent apoptosis, we evaluated the optimal concentration of the CI inhibitor rotenone. Complex I enzyme activity was measured according to ref 26. Cell viability was determined by trypan blue staining. To test for apoptosis, we checked for DNA laddering on a 1.5% agarose gel.

Cell Harvesting for Metabolomics

The growth medium was removed, and cells were rapidly rinsed by gently dispensing 5 mL of ice-cold 1× PBS onto the cell's surface. Then, 1 mL of ice-cold water was added into the flask, which was then flash frozen in liquid nitrogen. The time frame between medium removal and flash freezing was 1 min. Cells were detached with a cell scraper and transferred into a 15 mL tube. All cell suspensions were lysed by two rapid freeze–thaw cycles in liquid nitrogen, followed by 30 s of sonication on ice.²⁷

Metabolite Extraction

The final ratio of solvents used in the biphasic methanol/chloroform/water extraction method was 2.0:2.0:1.8.²⁸ Eight milliliters per gram of cold methanol (−20 °C) and 4 mL/g chloroform (type II carcinogen) were added to the homogenates and vortexed. Samples were always kept on ice, mixed for 10 min at 4 °C, and centrifuged for 5 min at 2000g at 4 °C to remove debris and precipitated protein. The pellet can be used to isolate DNA or proteins to serve as a normalization tool for the amount of sample deployed. The supernatant was transferred to a new tube, and 4 mL/g chloroform and 4 mL/g water were added. Samples were vortexed for 60 s, kept on ice for 10 min for phase separation, and centrifuged for 10 min at 2000g at 4 °C. The resulting upper polar and lower nonpolar fractions were separately transferred and combined (tests have shown that most of the metabolites, at least to some extent, are present in both fractions; data not shown) in three clean tubes containing the internal standard chloramphenicol, dedicated for subsequent analysis by using MeOH, ACN, and H₂O as alternative solvents

for LC–MS runs. Samples were lyophilized in the centrifugal concentrator.

Metabolite Sample Preparation for LC–MS/MS Analysis

The residuals were suspended in 35 μ L of ACN with 0.1% FA and 35 μ L of MeOH with 0.1% FA for analysis by HILIC and in 20 μ L of H₂O with 0.1% FA for RPLC and were then centrifuged at 17 500g for 5 min at 4 °C. Samples can be further cleaned to avoid column clogging, if necessary (iso-disc filters PTFE 13 mm × 0.2 mm, Supelco, Bellafonte, PA, USA). The supernatants were transferred to microvolume inserts, and 5 μ L per run was injected for LC–MS/MS analysis.

Rotenone- and mock-treated HeLa cells were run as biological triplicates. A total of 10 different run conditions (including polarity switch) were necessary to analyze all metabolites. A biological triplicate can be run automatically in 1 day. The scheduled MRM algorithm, monitoring transitions only 300 s around the expected RT, was used to decrease the number of concurrent MRMs monitored at any time point.

LC Conditions for Metabolomics

The chromatographic separations were performed on RP and zicHILIC stationary phases. A 1290 series UHPLC (Agilent, Santa Clara, CA, USA) with four different buffer conditions was used: (A1) 10 mM ammonium acetate in LC–MS grade H₂O (adjusted with FA to pH 3.5), (A2) 10 mM ammonium acetate in LC–MS grade H₂O (adjusted with ammonium hydroxide to pH 7.5), (B1) LC–MS grade ACN with 0.1% FA, and (B2) LC–MS grade MeOH with 0.1% FA. Gradients and flow conditions are described in Supporting Information Table S1. The columns have to be equilibrated with a blank run in the corresponding buffer system; in the case of MeOH-based methods, three blank runs were necessary for equilibrating.

Evaluation of the MRM Method and Data Analysis

Relative quantification was performed using MultiQuant software v.2.1.1 (AB Sciex, Foster City, CA, USA). Integration settings were a Gaussian smooth width of 2 points and a peak splitting factor of 2. Peak integrations were reviewed manually, and result tables were exported as Excel files. The most important feature used to correctly identify analytes was the ratio between the transitions, which had to match to MRM ion ratios of the corresponding tuned metabolites. The transition with the largest peak area was set to 1; transitions with smaller areas were divided by the largest. A shift of $\pm 10\%$ of the peak area was allowed for MRM ion ratios compared to the tuned value of the largest peak. All three transitions had to co-occur at the expected retention time and feature the same peak shape. Peak areas in blank runs had to be at least <90% smaller compared to that in the biological sample. The S/N ratio had to be above 10, at least for one transition. Transitions with a S/N ratio below 10 were used only for identification and not for quantification.

The significance of concentration differences in metabolite levels between controls and treated samples was evaluated using a two-tailed Student's *t*-test with a significance threshold of *p* < 0.05. The average ratio from all MRMs of one metabolite was used to calculate the log₂ fold change between treated and mock-treated samples. GraphPad Prism 5.03 was used for graphing, curve smoothing, and data organization.²⁹ The heat map was generated with R, which is available online at <http://www.r-project.org/> (Vanderbilt University, Nashville, TN, USA). MS² spectra of IMP were searched against the MassBank database.³⁰

Cell Harvesting and Sample Preparation for Proteomics

HeLa cells were harvested, lysed, and reduced in buffer containing 4% SDS, 0.1 M DTT, 0.1 M Tris, pH 8. A BC assay (Sigma-Aldrich) was performed to determine the protein concentration. Lysates (each containing 1 mg of protein) were sonicated on ice for 15 s and boiled at 95 °C for 5 min. Lysates were alkylated with a final concentration of 5.5 mM chloroacetamide for 30 min. Samples were precipitated with acetone overnight at -20 °C. Precipitates were lyophilized and dissolved in 8 M urea and 10 mM Tris, pH 8. Lys-C digestion (0.8 μ g/sample) was performed for 4 h at room temperature followed by a trypsin digestion (2 μ g/sample) in 2 M urea overnight at 37 °C.³¹ Peptides were purified with C18 columns and further separated using strong anion exchange chromatography (3M Purification, CT, USA) according to ref 32. Each sample was fractionated into six samples according to pH (11, 8, 6, 5, 4, and 3) and subsequently purified and concentrated with C18 StageTips. Each sample fraction was dissolved in 3 μ L of 5% ACN and 2% FA and analyzed by liquid chromatography online-coupled to a nanoHPLC–MS/MS system.

LC–MS Settings for Proteomics

LC–MS/MS was carried out by nanoflow reverse-phase liquid chromatography (Dionex Ultimate 3000, Thermo Scientific) coupled online to a Q-Exactive Plus Orbitrap mass spectrometer (Thermo Scientific). Briefly, LC separation was performed using a PicoFrit analytical column (75 μ m ID × 25 cm long, 15 μ m Tip ID (New Objectives, Woburn, MA, USA)) in-house packed with 3 μ m C18 resin (Reprosil-AQ Pur, Dr. Maisch, Germany). Peptides were eluted using a gradient from 3.8 to 98% solvent B over 192 min at a flow rate of 266 nL/min (solvent A: 0.1% formic acid in water; solvent B: 80% acetonitrile and 0.08% formic acid). Three kilovolts was applied for nanoelectrospray generation. A cycle of one full FT scan mass spectrum (300–1700 *m/z*, resolution of 35 000 at *m/z* 200) was followed by 12 data-dependent MS/MS scans with a normalized collision energy of 25 eV. Target ions already selected for MS/MS were dynamically excluded for 10 s.

Label-Free Proteomics Data Analysis

Raw MS data were processed with MaxQuant software (version 1.5.0.0)³³ and searched against the human proteome database UniProtKB with 81 194 entries, released 2012-02. A false discovery rate (FDR) of 0.01 for proteins and peptides and a minimum peptide length of 7 amino acids were required. A maximum of two missed cleavages was allowed for the tryptic digest. Cysteine carbamidomethylation was set as fixed modification, whereas N-terminal protein acetylation and methionine oxidation were set as variable modifications. The software MaxLFQ, a generic method for label-free quantification²³ that is integrated into MaxQuant, was used for relative quantification. Additionally, the match between runs feature was implemented to increase the number of peptides that can be used for quantification. The correlation analysis of biological replicates and the calculation of significantly different proteins were done with Perseus software (version 1.5.0.8). LFQ intensities (originating of at least two different peptides per protein group) were log-transformed, and only protein groups with values in every replicate were used for further data evaluation. In order to identify significantly different regulated proteins in control versus rotenone treatment, we applied a *t*-test with a permutation-based FDR. Two-hundred fifty permutations were performed; the FDR cutoff value was set to 0.05. The MaxQuant

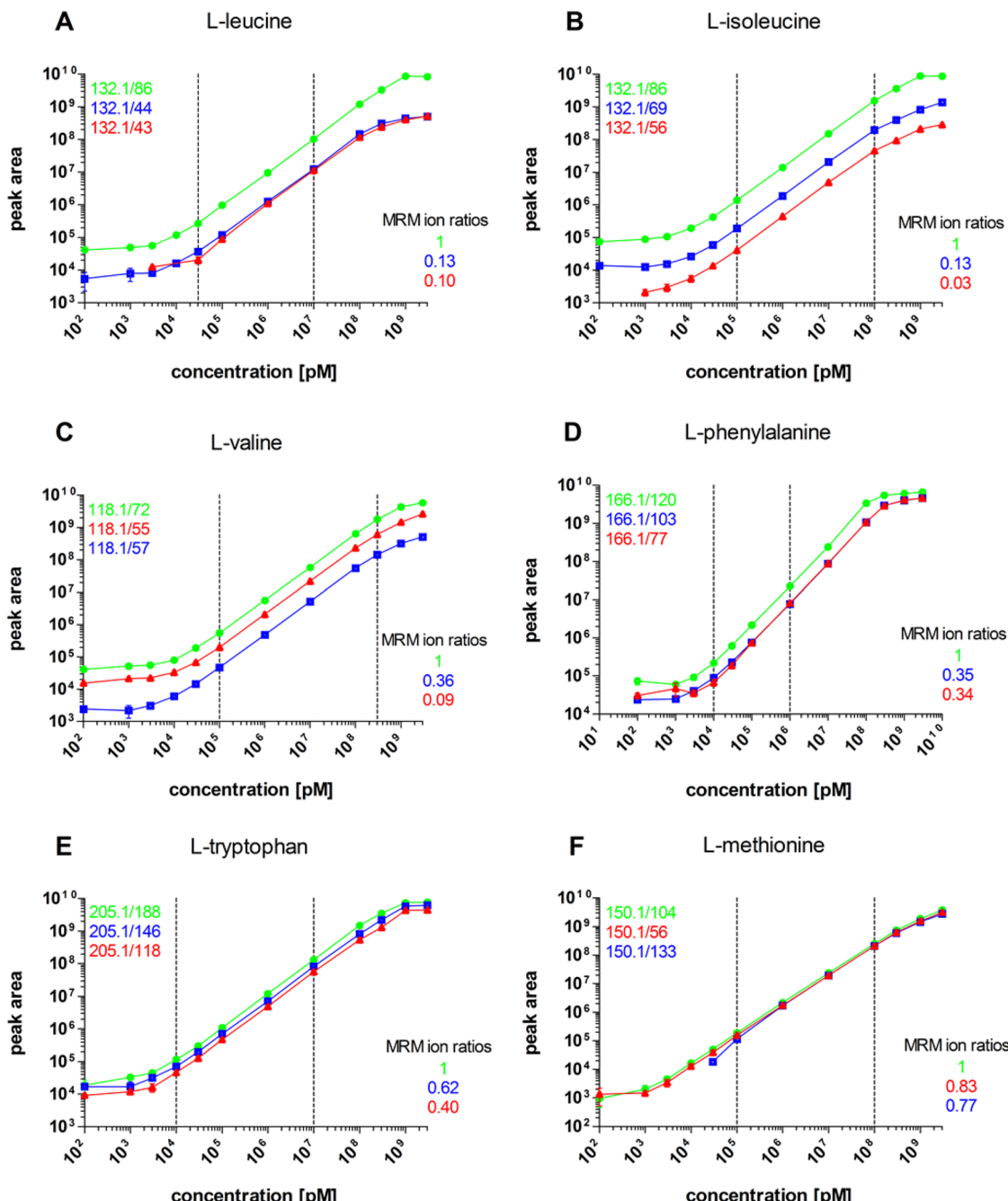


Figure 1. Dynamic range of six amino acids featuring three specific MRMs and their MRM ion ratios in logarithmic-scaled graphs. Data are the mean \pm SD; $n = 3$. The MRM ion ratios within the linear range (between dotted lines) are shown in brackets (transition–CV%): (A) L-leucine (86/44–5.06%; 86/43–16.02%), (B) L-isoleucine (86/69–2.96%; 86/56–4.35%), (C) L-valine (72/55–3.05%; 72/57–3.3%), (D) L-phenylalanine (120/77–7.68%; 120/103–7.05%), (E) L-tryptophan (188/146–3.6%; 188/118–3.25%), and (F) L-methionine (104/56–1.81%; 104/133–11.75%). The linear range of MRM ion ratios is highlighted with dotted lines.

processed output file can be found in Supporting Information Table S3.

Pathway and Network Analysis

Pathway and network analyses are novel methods to understand the complex data sets derived from deep omics studies. Pathway analysis was carried out by Gene Set Enrichment Analysis (GSEA) v2.0.14, with standard settings and a minimum size of 5 sets,³⁴ to address the question which pathways are altered upon rotenone treatment on a global scale. All mean values of the 3423 protein group ratios, as listed in Supporting Information Table

S4, were used as input for GSEA analysis. Both the *p*-value and FDR *q*-value had to be ≤ 0.05 to be regarded as significant.

To identify the main hub proteins in CI deficient cells, we used only significantly regulated (Supporting Information Table S5) as well as more than 2-fold regulated proteins (Supporting Information Table S4) to generate interaction networks using STRING 9.1 (Search Tool for the Retrieval of Interacting Genes),³⁵ applying a medium confidence score of 0.4. GO biological processes were selected within the network to visualize pathway affiliations. These interaction networks were extracted, further analyzed, and evaluated using the Cytoscape v3.1.1³⁶

plugin network analyzer.³⁷ Network analyzer was used to identify the hub proteins carrying the highest closeness centrality (CC) and betweenness centrality (BC) as key topological parameters.

RESULTS AND DISCUSSION

CI deficiency is the most common mitochondrial disease in humans.^{38,39} Here, we report a proteome and metabolome profiling study to shed light on molecular changes in CI deficient HeLa cells. For metabolome profiling, we adopted a strategy used in targeted MRM-based proteomics, which is not yet widespread in metabolomics: the use of multiple fragment masses and their ion ratios as an additional quality criterion for metabolite identification and relative quantification. After tuning and optimizing MS parameters for each of the 273 pure metabolites (except for acylcarnitines), we selected the three best transition's after LC separation on different columns. Besides the coelution of MRMs, we calculated their MRM ion ratios as a second layer of confirmation. Identification and relative quantification of metabolites from biological samples was approved if both criteria matched the tuned values. For proteomics profiling, we used a shotgun approach with relative label-free quantification. The proteome profiling results will be discussed together with the metabolome outcome for a holistic view of CI deficiency.

Evaluation of MRMs and MRM Ion Ratios

The mammalian metabolome consists of several thousand different metabolites,⁴⁰ which are chemically very diverse, and the abundances are spread over a wide range of magnitudes. Thus, profiling an entire metabolome remains a major challenge. Monitoring one MRM over the entire time range usually results in several peaks. Knowledge of the expected retention time (t_R) is essential for correct peak selection. However, especially in complex samples, two or more peaks close to the expected retention time are frequently detected. The correct peak often cannot be readily assigned, which can result in misidentification and incorrect quantification. One can calculate a relative retention time based on internal standards, but if two metabolites are indistinguishable based on MRMs and retention time, then only an MRM ion ratio alteration would identify this discordance.

To test the accuracy and dynamic range of our approach, an amino acid mixture consisting of pure Leu, Ile, Val, Phe, Trp, and Met was examined in technical triplicates. The concentrations ranged from 100 pM to 3 mM. The verification of linearity was determined by the limit of detection (LOD), the variation coefficient (CV%) of the technical triplicates, the MRM ion ratios, and Mandel's fitting test performed at 95% confidence level. The linear range of the amino acid set was determined to be below 15% CV (for MRMs and MRM ion ratios) of blank-corrected triplicates. With these criteria, the dynamic range spans about 3 to 4 orders of magnitude (Figure 1).

We next asked whether MRM ion ratios are robust indicators for metabolite identification and monitored several metabolites over a time range of 6 months in biological samples of different origin (cell culture, brain, liver, fat) and species (human, rat, mouse), as indicated in Table 1. MRM ion ratios not matching tuned reference values (Supporting Information Table S2) have to be removed to avoid false metabolite identification. Thus, MRMs together with their MRM ion ratios present an unmatched identification mark for metabolites. Pure metabolites (Figure 1), or with a biological matrix (Table 1), did not show any differences in their MRM ion ratios, indicating the robustness of this approach.

Table 1. Determination of the Variation of the MRM Ion Ratios of Various Sources Measured over 6 Months^a

	(1) MRM ion ratio	CV (%)	(2) MRM ion ratio	CV (%)
L-arginine ($n = 6$)	1/0.35	5.1	1/0.31	1.1
L-glutathione (red.) ($n = 5$)	1/0.35	9.6	1/0.31	10.6
creatinine ($n = 5$)	1/0.27	4.7	1/0.03	26.9
trimethylamine-N-oxide ($n = 6$)	1/0.66	4.7	1/0.12	8.9
NAD ($n = 6$)	1/0.53	5.2	1/0.26	9.7
FAD ($n = 6$)	1/0.48	3.3	1/0.39	3.1
sphingosine-1-phosphate ($n = 6$)	1/0.10	13.7	1/0.09	15.5

^aMRM values are according to Supporting Information Table S2.

Together, these results clearly show the accuracy and reproducibility of MRM ion ratios and can therefore be used for metabolite identification and relative quantification in complex mixtures.

Identifying Inosine 5'-Monophosphate by Applying MRM Ion Ratios

Inosine 5'-monophosphate (IMP) is the ribonucleotide of hypoxanthine and is the first compound formed during purine synthesis. IMP has the monoisotopic precursor molecular weight of 348.05 Da. The scheduled LC–MS/MS run for IMP detects two peaks at the proposed t_R , each showing all three MRMs (Figure 2).

There are no obvious criteria that assign the correct peak to IMP. Indeed, the 17-fold more intense peak shown on the right side is likely to be selected as the IMP-specific peak (Figure 2A). However, zooming into the left peak shows (Figure 2B) that the MRM ion ratios are clearly distinguishable from those of the peak on the right side. Comparing these MRM ion ratios with predetermined values shown in Supporting Information Table S2 allows one to unambiguously determine the peak on the left as the genuine signal for IMP. This was further confirmed by MS^2 spectra (Figure 2C–E).

Complex I Enzyme Activity, Cell Viability, and Apoptosis Upon Treatment of Rotenone

Most cancer cell lines feature alterations in their karyotype and switch their energy metabolism from a low rate of glycolysis followed by cellular respiration to a high rate of glycolysis followed by lactic acid fermentation, known as the Warburg effect. Thus, cancer cell lines are convenient, but they are not the optimal choice for studying the respiratory chain. Besides these limitations, our HeLa cells showed high cellular respiration (Supporting Information Figure S1A), comparable to that of other noncancerous tissues, like renal tissue.^{26,41}

We examined the efficiency of several rotenone concentrations, ranging from 10 nM to 1 μ M, to inhibit CI enzyme activity. CI enzyme activity of HeLa cells was entirely inhibited at a concentration of 1 μ M rotenone (Supporting Information Figure S1A). At the same time, the cell viability was over 90% (Supporting Information Figure S1B), and no apoptosis-specific DNA laddering was detected (Supporting Information Figure S1C).

Metabolome Profile of Rotenone-Treated HeLa Cells

We applied the MRM ion ratio strategy to identify differences in metabolite abundance in CI deficient HeLa cells using rotenone, a potent inhibitor of NADH dehydrogenase. After 38 h of incubation with 1 μ M rotenone, 143 out of 273 metabolites were

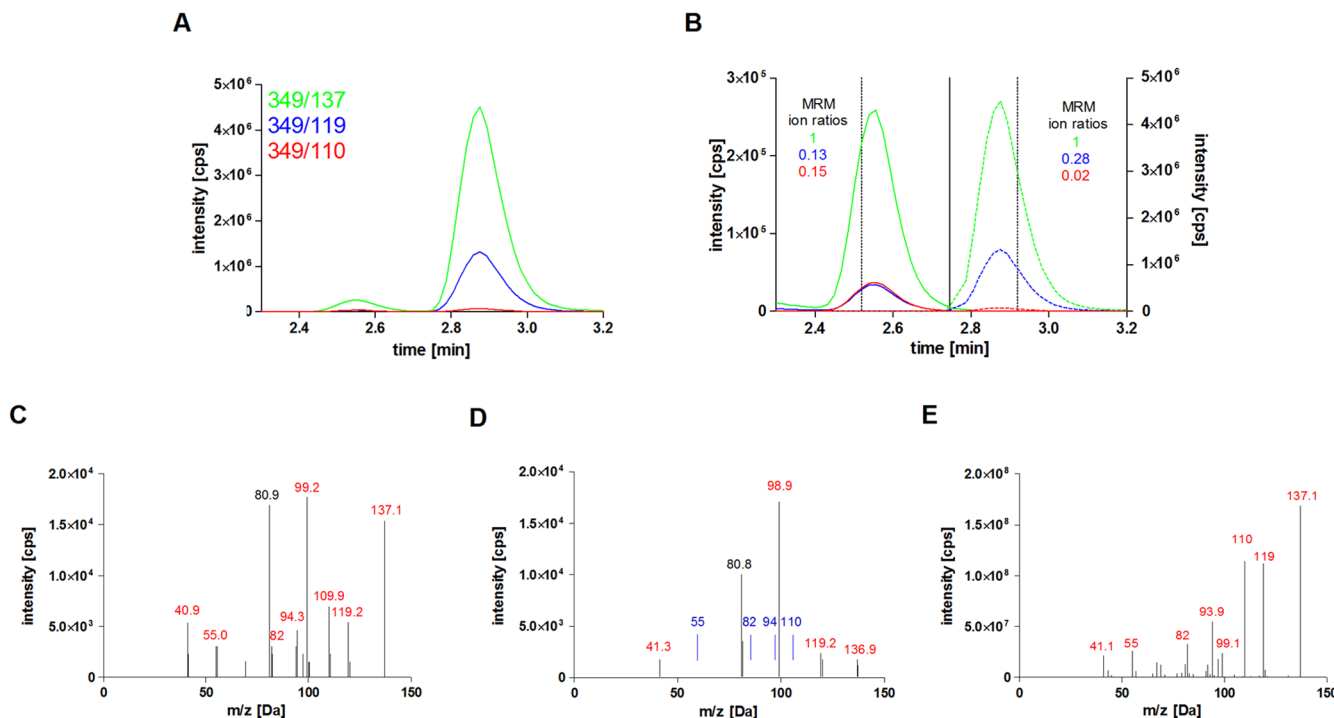


Figure 2. An example of correct peak identification based on MRM ion ratios. Inosine 5'-monophosphate (IMP) with a monoisotopic precursor molecular weight of 348.05 Da was monitored by the following three MRM transitions in positive ionization mode: 137, 119, and 110 Da. (A) Illustration of IMP-specific MRM only in a time frame of the expected t_R . Both peaks feature all three MRM and could be identified as correct; the mean area of the right peak is 17 times larger than that of the left peak. (B) Only MRM ion ratios identify the peak on the left side as truly being IMP (zoomed y axis), matching the tuned IMP ratios of 1/0.13/0.12. The peak on the right side has different MRM ion ratios, 1/0.28/0.02, and hence does not match IMP. Dotted lines at minutes 2.52 and 2.92 mark the time points where MS² spectra were taken. (C) MS² spectrum to verify that the left peak is IMP; (D) the peak on the right side could not be assigned to any metabolite. (E) Tuned IMP spectra as a reference; all MS² spectra were taken with a CE of 73 V. Fragment masses shown in red are identical to tuned IMP; missing fragment masses are shown in blue.

detected with at least 2 transitions and 3 measured values per condition (Supporting Information Table S6). Metabolites featuring different MRM ion ratios ($\pm 10\%$), compared to the ratios obtained during MRM ion ratio determination using individual standards (Supporting Information Table S2), were excluded. Metabolites with significantly (t -test; $p < 0.05$) different concentrations between control cells and rotenone-treated cells and at least a 2-fold change are shown in Figure 3.

We found that the abundance of 23 of the 143 detected metabolites significantly changed in response to rotenone treatment. Three metabolites were upregulated (>2.6-fold) and 20 metabolites downregulated (<0.45-fold) in rotenone-treated samples. Interpretation of altered metabolite ratios is, in general, challenging, as many compounds co-occur in different pathways.

We were able to identify important metabolites of the oxidative phosphorylation system as being significantly regulated upon rotenone treatment, such as flavin adenine dinucleotide (FAD), a condensation product of flavin mononucleotide (FMN), and adenosine diphosphate (ADP), which were both downregulated (Figure 3 and Supporting Information Table S6). FMN functions as an electron acceptor during the oxidation of NADH to NAD⁺ in CI of the respiratory chain. Rotenone blocks the ubiquinone-binding site. Consequently, the electron transfer via FMN to coenzyme Q10 is prevented, and the entire oxidative phosphorylation chain is interrupted, explaining the observed downregulation of FMN upon rotenone treatment (Figure 3). FAD is a prosthetic group in the enzyme complex succinate dehydrogenase (complex II) that oxidizes succinate to fumarate within the tricarboxylic acid cycle (TCA). The electron carrier nicotinamide adenine dinucleotide phosphate (NADP⁺) is

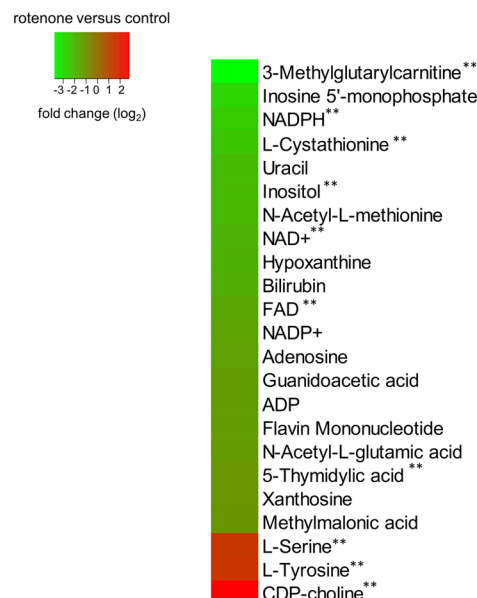


Figure 3. Metabolic profile of significantly regulated metabolites in rotenone-treated versus control cells. Only significantly ($p < 0.05$) and >2-fold changed metabolites are shown; **, p -value < 0.01.

downregulated in the oxidized (NADP⁺) as well as in the reduced (NADPH) form (Figure 3). NADPH provides the reducing equivalents for biosynthetic reactions and participates in the oxidation-reduction involved in protection from reactive oxygen species (ROS).

Nicotinamide adenine dinucleotide (NAD^+) is used in glycolysis and the TCA cycle and was significantly downregulated in rotenone-treated cells (Figure 3). NADH serves as an electron carrier by being alternately oxidized (NAD^+) and reduced (NADH), and the reducing potential stored in NADH can be converted to ATP through the electron transport chain. The final end product, the chemical energy transporter adenosine triphosphate (ATP) of the OXPHOS system, was not detectable, but adenosine diphosphate (ADP) was significantly downregulated (Figure 3).

Bilirubin, a degradation product of heme, which is the central part in Fe–S clusters, was significantly downregulated as well.

CDP-choline has been shown to restore the activity of mitochondrial ATPase and membrane Na^+/K^+ ATPase and has a neuroprotective effect under hypoxic and ischemic conditions, at least in neurodegeneration models.⁴² Such a mechanism could explain the observed 7-fold elevated level of CDP-choline in our rotenone-treated samples. This result is further supported by the findings from our proteome profile, which detected a 4-fold upregulation of choline-phosphate cytidylyltransferase A (PCYT1A), which catalyzes the synthesis of CDP-choline: cytidine triphosphate + phosphorylcholine → pyrophosphate + CDP-choline.

Most of the metabolites were highly regulated, but not significantly, due to a high metabolic flux and the low number of replicates. Nevertheless, the TCA cycle showed dramatically reduced metabolite levels, which was the lowest for citric acid, with a more than 100-fold decrease, and cis-aconitic acid, with a 6-fold reduction, virtually shutting down the TCA cycle (Supporting Information Table S6).

All QTrap wiff files can be downloaded via <http://www.peptideatlas.org/PASS/PASS00543>. A MultiQuant processed list of all detected metabolite ratios can be found in Supporting Information Table S6.

Proteome Profile of Rotenone-Treated HeLa Cells

The same cell culture conditions as those described for metabolome profiling were used to determine changes in the proteome upon CI inhibition. For proteome profiling, we additionally fractionated the samples using strong anion exchange chromatography of tryptic peptides prior to online coupled LC–MS/MS separation of peptides. Thus, six samples (3 biological replicates) were analyzed in a total of 42 LC–MS/MS runs. We identified more than 1.5×10^6 MS² spectra, belonging to 6075 protein groups in total. For further data analyses, we used protein groups with LFQ intensities in each replicate. This criterion resulted in a final protein group list with 3424 entries. Raw data can be downloaded via: <http://www.peptideatlas.org/PASS/PASS00543>. MaxQuant processed output files can be found in Supporting Information Table S3.

The reproducibility of the biological replicates was tested by Pearson correlation and visualized in a multiscatter plot (Supporting Information Figure S2A,B). The Pearson correlation was consistently >0.93 , indicating a robust quality of the replicates.

To identify significantly altered protein groups, the distribution between the sample cohorts was visualized in a volcano plot (Figure 4). Forty six protein groups were found to be significantly regulated (26 up; 20 down) in rotenone-treated cells (Supporting Information Table S5).

Pathway Analysis of CI Deficient Cells

First, we aimed to identify regulated pathways on a global scale in CI deficient HeLa cells. Therefore, we applied GSEA, a

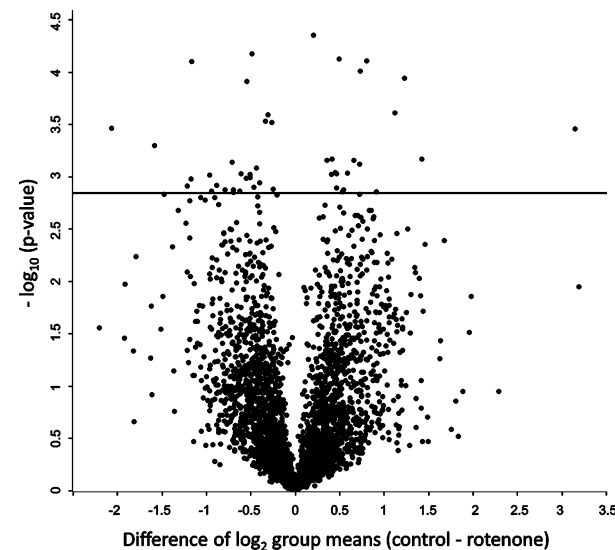


Figure 4. Volcano plot showing proteome data and the mean difference of LFQ intensities between controls and rotenone-treated cells versus statistical significance ($-\log_{10}$ of the p -value). The line shows where the threshold was set by applying a FDR of 0.05, resulting in 46 significantly regulated protein groups.

computational method that determines whether an a priori defined set of genes shows statistically significant, concordant differences between two biological states.

We showed that OXPHOS-related metabolites were downregulated; in contrast, corresponding proteins were dysregulated. The ATP synthase H⁺ transporting subunits, for example, were upregulated. This can be explained by the reverse direction of the ATPase, where protons are pumped into the mitochondrial interspace by hydrolyzing ATP.^{43,44} An electrochemical gradient is essential for several biological functions. Another 14 respiratory chain subunits were upregulated, and 28 were downregulated (Supporting Information Figure S3). An explanation for the dysregulation could be the fact that the subunits for the ATPase are encoded by two different genomes. Furthermore, the assembly and oligomerization of the multi-subunit containing enzyme ATPase happens in several steps,⁴⁵ and intermediate complexes for H⁺ transport might be differentially regulated. These results attest to the complex regulation of this system, where compensatory effects and regulatory feedback loops play a role.

In contrast, a study analyzing the gene expression using a low dose of rotenone (5 nM) reported an increase of cellular energy metabolism gene transcripts, based on GSEA results (note that the FDR p -values were over 0.15; our cutoff was <0.05).³

We found that the pentose-phosphate pathway (PPP), galactose metabolism, and glycolysis and gluconeogenesis were significantly downregulated (Supporting Information Table S7, based on KEGG). Furthermore, glutathione metabolism, cell adhesion, and the ribosome were significantly downregulated in CI deficient cells.

PPP provides reducing equivalents in the form of NADPH for antioxidant defense; our study shows significantly reduced glutathione metabolism and about 2-fold decreased levels of glutathione (GSH) and oxidized glutathione (GSSG) as well as 10-fold decreased levels of NADPH (Supporting Information Table S6).

Porphyrin metabolism was downregulated as well (FDR value 0.094), including cytochrome c-type heme lyase (HCCS), the

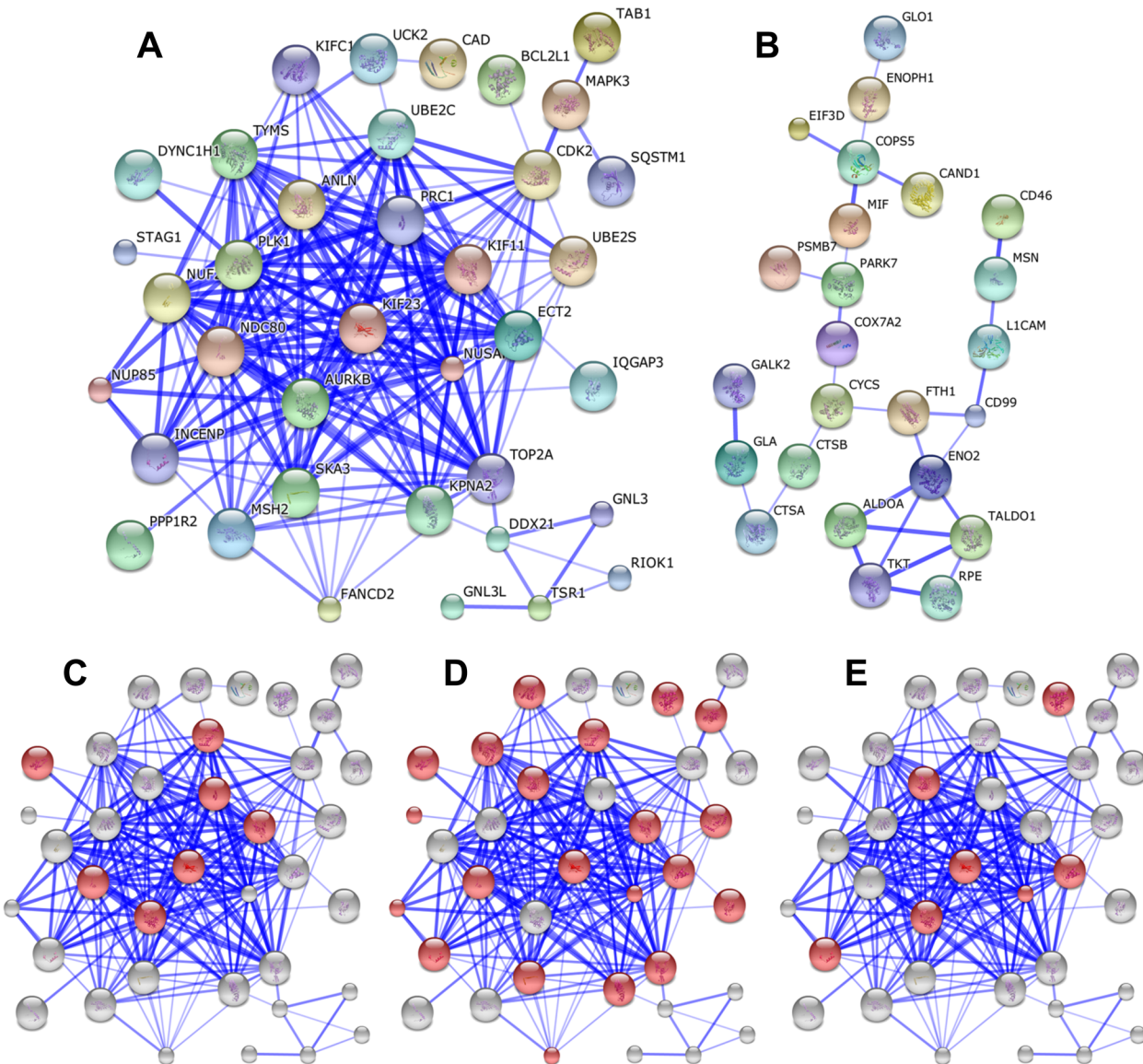


Figure 5. String network and pathway analysis of significant and/or 2-fold regulated proteins upon rotenone treatment. Unconnected nodes have been removed. (A) Upregulated and (B) downregulated networks. (C–E) Network from panel A with proteins of the following GO pathways highlighted in red: (C) spindle organization, (D) cell cycle, and (E) cytokinesis.

protein that covalently links the heme group to the apoprotein of cytochrome c and coproporphyrinogen-III oxidase (CPOX), involved in heme biosynthesis.

The only significantly upregulated pathways were the cell cycle and cytokinesis (Supporting Information Table S7, based on Gene Ontology).

Network Analysis and Hub Protein Identification: Upregulation of Proteins Involved in Cytokinesis, Cell Cycle, and the Spindle and Downregulation of Cytoskeleton upon CI Inhibition

The interaction network of upregulated proteins upon rotenone treatment is visualized in Figure 5A, showing one main cluster of proteins. GO pathway analysis within this network revealed that the proteins of this cluster are involved in mitotic spindle dynamics (Figure 5C), cell cycle (Figure 5D), and cytokinesis (Figure 5E). The most important hub proteins extracted from this network, are listed in Table 2 along with an additional pertinent description of their function.

The network analysis revealed a role of cyclin-dependent kinase 2 (CDK2), a serine/threonine-protein kinase and master regulator of mitotic events, as the main hub protein with the highest BC value. The six top hub proteins, DNA topoisomerase 2-alpha (TOP2A), importin subunit alpha-1 (KPNA2), aurora kinase B (AURKB), serine/threonine-protein kinase PLK1 (PLK1), kinesin-like protein KIF11 (KIF11), and ubiquitin-conjugating enzyme (UBE2C), all have CC values above 0.59 and BC values above 0.05 and are all important players in the cell cycle.

If we take a closer look at the compelling upregulation of proteins involved in the regulation of the mitotic spindle (Figure 5C), then we find AURKB, a component of the chromosomal passenger complex, which has essential functions at the centromere in ensuring correct chromosome alignment and segregation.⁴⁶ Two kinases, AURKB and PLK1, both regulate protein regulator of cytokinesis 1 (PRC1),⁴⁷ a key regulator of cytokinesis, controlling the spatiotemporal formation of the midzone during the metaphase to anaphase transition.⁴⁸ UBE2C

Table 2. Key Hub Proteins Based on Topological Parameters Betweenness and Closeness Centrality of the String Network of Differentially Expressed Proteins upon Rotenone Treatment

protein	protein name	degree	closeness centrality	betweenness centrality	function (extracted from uniprot.org)
Significant and/or 2-Fold Upregulated Proteins upon Rotenone Treatment					
CDK2	Cyclin-dependent kinase 2	18	0.6	0.210	cell cycle
TOP2A	DNA topoisomerase 2-alpha	20	0.643	0.135	segregation of daughter chromosomes
KPNA2	Importin subunit alpha-1	18	0.621	0.114	functions in nuclear protein import
AURKB	Aurora kinase B	22	0.621	0.100	correct chromosome alignment and segregation
PLK1	Serine/threonine-proteinkinase	22	0.621	0.100	key regulator of cytokinesis
KIF11	Kinesin-like protein KIF11	21	0.61	0.060	required for establishing a bipolar spindle
UBE2C	Ubiquitin-conjugating enzyme	18	0.59	0.055	essential factor of the anaphase promoting complex/cyclosome
TYMS	Thymidylate synthase	18	0.59	0.055	mitochondrial thymidylate biosynthesis pathway
NUF2	Kinetochore protein Nuf2	20	0.6	0.016	required for kinetochore integrity
NDC80	Kinetochore protein NDC80 homologue	19	0.59	0.013	chromosome segregation and spindle checkpoint activity
NUSAP1	Nucleolar and spindle-associated protein 1	20	0.6	0.012	organization of mitotic spindle microtubules
KIF23	Kinesin-like protein KIF23	19	0.59	0.009	component of the centalspindlin complex
MSH2	DNA mismatch repair protein Msh2	14	0.529	0.008	component of the postreplicative DNA mismatch repair system
PRC1	Protein regulator of cytokinesis 1	19	0.59	0.008	key regulator of cytokinesis
ANLN	Actin-binding protein anillin	18	0.581	0.006	required for cytokinesis
INCENP	Inner centromere protein	15	0.522	0.004	key regulator of mitosis
ECT2	Protein ECT2	17	0.571	0.002	component of the centalspindlin complex
SKA3	Spindle and kinetochore-associated protein 3	16	0.529	0.002	essential for proper chromosome segregation
FANCD2	Fanconi anemia group D2 protein	9	0.468	0.001	required for maintenance of chromosomal stability
KIFC1	Kinesin-like protein KIFC1	9	0.439	0.000	required for bipolar spindle formation
Significant and/or 2-Fold Downregulated Proteins upon Rotenone Treatment					
CYCS	Cytochrome c	3	0.311	0.656	heme carrying key player of the respiratory chain
FTH1	Ferritin heavy chain	3	0.295	0.498	important for iron homeostasis
PARK7	Parkinson disease protein 7	3	0.261	0.466	plays a significant role in antioxidative defense
COPSS	COP9 signalosome complex subunit 5	4	0.202	0.320	cellular and developmental processes
ENO2	Gamma-enolase	5	0.261	0.300	glycolysis and gluconeogenesis
CD99	CD99 antigen	3	0.258	0.237	involved in T-cell adhesion processes
TALDO1	Transaldolase	4	0.217	0.042	balance of metabolites in the pentose-phosphate pathway
TKT	Transketolase	4	0.217	0.042	pentose phosphate pathway

is an essential factor of the anaphase promoting complex/cyclosome, where it attaches ubiquitin to other proteins.

Another hub proteins was kinetochore protein (NDC80), required for chromosome segregation and spindle checkpoint activity. Furthermore, the two kinesines, kinesin-like protein KIF23 (KIF23) and KIF11, are hub proteins. KIF23 is a component of the centalspindlin complex that serves in the microtubule-dependent and Rho-mediated signaling required for myosin contractile ring formation during cell cycle cytokinesis, whereas KIF11 is a motor protein required for establishing a bipolar spindle.

Several proteins involved in cytoskeleton organization were significantly downregulated, such as actin-related protein (ACTR3), mediating the formation of a branched actin network, gamma-adducin (ADD3), a membrane-cytoskeleton-associated protein that promotes the assembly of the spectrin–actin network, kinectin (KTN1), a receptor for kinesin-driven vesicle motility, and moesin (MSN) (Figure 5B), another protein involved in cellular movement (Supporting Information Table S5). This is in accordance with a previous study which showed that CI inhibition upon rotenone treatment leads to minor cytoskeletal changes.⁴

Which mechanisms are responsible for the observed increase of cell cycle and cytokinesis proteins and decrease of the cytoskeleton upon CI inhibition by rotenone?

Light and electron microscopic examinations of cells treated with rotenone revealed that chromosome, spindle, and centriole configurations were grouped in a spherical mass near the cell's center and that cells did not progress beyond the early stages of mitosis.⁵ It has been shown that rotenone has a CI-independent function, as it induces conformational changes in tubulin by directly binding to tubulin (*in vivo* and *in vitro*), which leads to perturbed chromosome alignment at the metaphase plate in which they do not properly attach to microtubules (MT) and form multipolar spindles.⁶

Others have shown that rotenone-induced cytotoxicity is mediated by MT destabilization⁷ and that dopaminergic neuron death induced by treatment with rotenone is independent of CI inhibition.⁴⁹

In addition, it has been reported that free radical generation in human neurons leads to the disruption and loss of the cytoskeleton.⁵⁰ Others suggest that upregulation of cell cycle proteins under oxidative stress is a well-orchestrated process of apoptosis, particularly in Alzheimer's disease.⁵¹ In contrast, a transcriptome study showed a downregulation of cell cycle genes upon rotenone treatment,² but RNA and protein expression are poorly correlated in general.^{3,31}

In summary, we think that the increase of key proteins necessary for the cell cycle could be a side effect of the depolymerization of MT, induced by binding of rotenone to

tubulin. The depolymerization of MT causes a cell cycle block during mitosis and leads to an overexpression of proteins to rescue mitosis, as detected in our study, and could therefore be regarded as being independent of CI dysfunction. However, if we consider a study that analyzed mtDNA depleted ρ^0 cells, which feature severe cytoskeletal alterations, like a collapsed vimentin network and a dense accumulation of mitochondria around the nucleus,⁴ then this indicates a potent role of the OXPHOS state per se. Many other proteins, like knocking down components of the fission and fusion machineries, not only affect ATP production but also impede cell cycle progression.⁵²

Therefore, we cannot conclude whether the OXPHOS status of the cell in general, rotenone's side target tubulin, or both are responsible for the upregulation of proteins involved in the cell cycle.

Downregulation of Iron–Sulfur Clusters in CI Deficient HeLa Cells

Mitochondria play an essential role in cellular iron homeostasis,⁵³ where iron is used for heme biosynthesis and the formation of iron–sulfur clusters (Fe–S). Protein complexes containing Fe–S clusters within the respiratory chain and TCA cycle are NADH-dehydrogenase, succinate dehydrogenase, cytochrome c-oxireductase (complex III), and aconitase dehydratase. In general, Fe–S clusters are involved in key biological processes such as electron transfer, DNA synthesis, and metabolic and regulatory processes.⁵⁴

In our study, transferrin receptor 1 (TFRC), responsible for the cellular uptake of iron, was found to be significantly upregulated, whereas the iron storage protein ferritin (FTH1) was significantly downregulated. In a former study with similar results, the upregulation of TFRC was explained by the transformation of aconitase (ACO1) activity into iron regulatory protein 1 (IRP1) activity upon the loss of Fe–S clusters. Because low iron conditions normally activate IRP1, its activation by decreased Fe–S clusters may give a false low iron signal.⁵⁴

The main downregulated hub proteins (Table 2) in rotenone-treated cells besides FTH1 were cytochrome c (CYCS) and cytochrome c oxidase subunit 7A2 (COX7A2). CYCS is a heme-carrying key player of the respiratory chain, which transfers electrons from complex III to cytochrome c oxidase (complex IV), where complex IV is the terminal oxidase in mitochondrial electron transport. As already mentioned in the Metabolome Profile of Rotenone Treated HeLa Cells section, bilirubin, a degradation product of heme, was significantly downregulated, showing a well-coordinated regulation of the proteome and metabolome. Together, these data strikingly show how an impaired CI affects heme and Fe–S clusters.

Another main hub protein is Parkinson disease protein 7 (PARK7). It plays a significant role in the antioxidant defense to protect cells from oxidative stress and is a potential biomarker for Parkinson's disease.⁵⁵ Exposure of naïve neuroblastoma cells to increasing concentrations of rotenone led to the upregulation of both the mRNA and protein levels of PARK7,⁵⁶ suggesting a differential response in tumor cells.

CI deficiency is associated with increased ROS levels, but the cellular context (e.g., cell type, cell metabolic state, culture conditions, external glucose concentration, cell immortalization) may quench and counteract such an increase.⁵⁷

According to our findings, the respiratory chain and the TCA cycle are completely failing to provide ATP for the cell: citrate levels are 100-fold downregulated. Our working hypothesis is that this lack of energy will be compensated by an upregulation of

glycolysis and PPP. Instead, these pathways were significantly downregulated as well. Thus, rotenone-treated cells have a serious energy problem and, additionally, their defense against ROS is severely compromised, as indicated by decreased glutathione metabolism, GSH, GSSG, and NADPH.

CONCLUSIONS

In the present study, we integrated metabolome and proteome profiles of rotenone-treated HeLa cells. For metabolite screening, we report a rapid, high confidence method for identification and relative quantification using up to three MRMs and their MRM ion ratios for robust and unambiguous analysis of complex samples.

We detected molecular changes in CI deficient cells by quantitatively analyzing targeted metabolomics and shotgun proteomics data, applying bioinformatics network approaches, and identified several biological pathways and hub proteins that are dysregulated in rotenone-treated HeLa cells. We showed that OXPHOS and the TCA cycle were shut down entirely in addition to significantly decreased glycolysis and PPP upon rotenone treatment. Furthermore, Fe–S clusters and glutathione metabolism were significantly downregulated, indicated by both metabolome and proteome data. We saw an enrichment of M-phase components, most likely due to an arrest at M-phase.

ASSOCIATED CONTENT

S Supporting Information

Figure S1: Determination of the CI enzyme activity, viability, and apoptosis rate of HeLa cells treated with different concentrations of rotenone: (A) CI enzyme activity in units/gram of protein versus the concentration of rotenone, (B) viability (percent of living/dead cells), and (C) agarose gel loaded with nuclear DNA showing no evidence of apoptosis. Figure S2: Multiscatter plot to test the reproducibility of LFQ intensities of all biological replicates for the proteome data: (A) Pearson correlation was >0.97 for controls and (B) >0.94 for rotenone-treated replicates. Figure S3: GSEA pathway analysis featuring dysregulation of proteins involved in the OXPHOS system. All subunits that are assigned to the REACTOME pathway (A) respiratory electron transport, (B) formation of ATP by chemiosmotic coupling, and (C) ion transport by P type ATPases. Black bars represent single subunits separated according to their \log_2 protein ratio on the heat map (red, upregulated in rotenone-treated samples; blue, downregulated). Table S1: HPLC running conditions for metabolome profiling. Table S2: List of all metabolites and their specific MRM instrument settings and MRM ion ratios. Table S3: MaxQuant output file of the proteome profile with LFQ intensities. Table S4: List of protein groups and LFQ intensities identified in every replicate. Table S5: List of significantly expressed proteins in CI deficiency. Table S6: List of all metabolite ratios between rotenone treatment and controls. Table S7: GSEA analysis of proteome data; list of significantly altered pathways of CI deficient cells. This material is available free of charge via the Internet at <http://pubs.acs.org>.

AUTHOR INFORMATION

Corresponding Author

*E-mail: meierhof@molgen.mpg.de. Phone: +49-30-8413-1567. Fax: +49-30-8413-1365.

Present Address

[†](I.G.) Freie Universität Berlin, Fachbereich Biologie, Chemie, Pharmazie, Takustraße 3, 14195 Berlin, Germany.

Notes

The authors declare no competing financial interest.

ACKNOWLEDGMENTS

We thank Beata Lukaszewska-McGreal for assistance during method development and Joachim Kopka (Max Planck Institute of Molecular Plant Physiology, Golm, Germany) for supplying most of the metabolites for tuning. We thank Peter Kaiser for fruitful discussion. This work is part of the Ph.D. thesis of I.G. This study was funded by the Max Planck Institute for Molecular Genetics, Berlin, Germany.

REFERENCES

- (1) Fassone, E.; Rahman, S. Complex I deficiency: clinical features, biochemistry and molecular genetics. *J. Med. Genet.* **2012**, *49*, 578–590.
- (2) Cabeza-Arvelaiz, Y.; Schiestl, R. H. Transcriptome analysis of a rotenone model of parkinsonism reveals complex I-tied and -untied toxicity mechanisms common to neurodegenerative diseases. *PLoS One* **2012**, *7*, e44700.
- (3) Greene, J. G.; Greenamyre, J. T.; Dingledine, R. Sequential and concerted gene expression changes in a chronic in vitro model of parkinsonism. *Neuroscience* **2008**, *152*, 198–207.
- (4) Annunen-Rasila, J.; Ohlmeier, S.; Tuokko, H.; Veijola, J.; Majamaa, K. Proteome and cytoskeleton responses in osteosarcoma cells with reduced OXPHOS activity. *Proteomics* **2007**, *7*, 2189–2200.
- (5) Barham, S. S.; Brinkley, B. R. Action of rotenone and related respiratory inhibitors on mammalian cell division. 2 Ultrastructural studies. *Cytobios* **1976**, *15*, 97–109.
- (6) Srivastava, P.; Panda, D. Rotenone inhibits mammalian cell proliferation by inhibiting microtubule assembly through tubulin binding. *FEBS J.* **2007**, *274*, 4788–4801.
- (7) Hongo, H.; Kihara, T.; Kume, T.; Izumi, Y.; Niidome, T.; Sugimoto, H.; Akaike, A. Glycogen synthase kinase-3β activation mediates rotenone-induced cytotoxicity with the involvement of microtubule destabilization. *Biochem. Biophys. Res. Commun.* **2012**, *426*, 94–99.
- (8) Betarbet, R.; Sherer, T. B.; MacKenzie, G.; Garcia-Osuna, M.; Panov, A. V.; Greenamyre, J. T. Chronic systemic pesticide exposure reproduces features of Parkinson's disease. *Nat. Neurosci.* **2000**, *3*, 1301–1306.
- (9) Lambert, A. J.; Brand, M. D. Inhibitors of the quinone-binding site allow rapid superoxide production from mitochondrial NADH:ubiquinone oxidoreductase (complex I). *J. Biol. Chem.* **2004**, *279*, 39414–39420.
- (10) Orr, A. L.; Ashok, D.; Sarantos, M. R.; Shi, T.; Hughes, R. E.; Brand, M. D. Inhibitors of ROS production by the ubiquinone-binding site of mitochondrial complex I identified by chemical screening. *Free Radical Biol. Med.* **2013**, *65*, 1047–1059.
- (11) Rhee, E. P.; Thadhani, R. New insights into uremia-induced alterations in metabolic pathways. *Curr. Opin. Nephrol. Hypertens.* **2011**, *20*, 593–598.
- (12) Taegtmeyer, H.; Heather, L. C.; Wang, X.; West, J. A.; Griffin, J. L. A practical guide to metabolomic profiling as a discovery tool for human heart disease. *J. Mol. Cell. Cardiol.* **2013**, *55*, 2–11.
- (13) Guo, B.; Chen, B.; Liu, A.; Zhu, W.; Yao, S. Liquid chromatography-mass spectrometric multiple reaction monitoring-based strategies for expanding targeted profiling towards quantitative metabolomics. *Curr. Drug Metab.* **2012**, *13*, 1226–1243.
- (14) Wei, R.; Li, G.; Seymour, A. B. High-throughput and multiplexed LC/MS/MRM method for targeted metabolomics. *Anal. Chem.* **2010**, *82*, 5527–5533.
- (15) Lu, W.; Clasquin, M. F.; Melamud, E.; Amador-Noguez, D.; Caudy, A. A.; Rabinowitz, J. D. Metabolomic analysis via reversed-phase ion-pairing liquid chromatography coupled to a stand alone orbitrap mass spectrometer. *Anal. Chem.* **2010**, *82*, 3212–3221.
- (16) Buré, C.; Ayciriex, S.; Testet, E.; Schmitter, J.-M. A single run LC-MS/MS method for phospholipidomics. *Anal. Bioanal. Chem.* **2013**, *405*, 203–213.
- (17) Bielawski, J.; Pierce, J. S.; Snider, J.; Rembiesa, B.; Szulc, Z. M.; Bielawska, A. Comprehensive quantitative analysis of bioactive sphingolipids by high-performance liquid chromatography-tandem mass spectrometry. *Methods Mol. Biol.* **2009**, *579*, 443–467.
- (18) Preinerstorfer, B.; Schiesel, S.; Lämmerhofer, M.; Lindner, W. Metabolic profiling of intracellular metabolites in fermentation broths from beta-lactam antibiotics production by liquid chromatography-tandem mass spectrometry methods. *J. Chromatogr. A* **2010**, *1217*, 312–328.
- (19) Bueno, M. J. M.; Agüera, A.; Gómez, M. J.; Hernando, M. D.; García-Reyes, J. F.; Fernandez-Alba, A. R. Application of liquid chromatography/quadrupole-linear ion trap mass spectrometry and time-of-flight mass spectrometry to the determination of pharmaceuticals and related contaminants in wastewater. *Anal. Chem.* **2007**, *79*, 9372–9384.
- (20) Gros, M.; Petrović, M.; Barceló, D. Tracing pharmaceutical residues of different therapeutic classes in environmental waters by using liquid chromatography/quadrupole-linear ion trap mass spectrometry and automated library searching. *Anal. Chem.* **2009**, *81*, 898–912.
- (21) Schürmann, A.; Dvorak, V.; Crüzer, C.; Butcher, P.; Kaufmann, A. False-positive liquid chromatography/tandem mass spectrometric confirmation of sebutylazine residues using the identification points system according to EU directive 2002/657/EC due to a biogenic insecticide in tarragon. *Rapid Commun. Mass Spectrom.* **2009**, *23*, 1196–1200.
- (22) Kushnir, M. M.; Rockwood, A. L.; Nelson, G. J.; Yue, B.; Urry, F. M. Assessing analytical specificity in quantitative analysis using tandem mass spectrometry. *Clin. Biochem.* **2005**, *38*, 319–327.
- (23) Cox, J.; Hein, M. Y.; Luber, C. A.; Paron, I.; Nagaraj, N.; Mann, M. MaxLFQ allows accurate proteome-wide label-free quantification by delayed normalization and maximal peptide ratio extraction. *Mol. Cell. Proteomics* **2014**, M113.031591.
- (24) Smith, C. A.; O'Maille, G.; Want, E. J.; Qin, C.; Trauger, S. A.; Brandon, T. R.; Custodio, D. E.; Abagyan, R.; Siuzdak, G. METLIN: a metabolite mass spectral database. *Ther. Drug Monit.* **2005**, *27*, 747–751.
- (25) Wishart, D. S.; Jewison, T.; Guo, A. C.; Wilson, M.; Knox, C.; Liu, Y.; Djoumbou, Y.; Mandal, R.; Aziat, F.; Dong, E.; et al. HMDB 3.0—The Human Metabolome Database in 2013. *Nucleic Acids Res.* **2013**, *41*, D801–D807.
- (26) Mayr, J. A.; Meierhofer, D.; Zimmermann, F.; Feichtinger, R.; Kögl, C.; Ratschek, M.; Schmeller, N.; Sperl, W.; Kofler, B. Loss of complex I due to mitochondrial DNA mutations in renal oncocytoma. *Clin. Cancer Res.* **2008**, *14*, 2270–2275.
- (27) Bi, H.; Krausz, K. W.; Manna, S. K.; Li, F.; Johnson, C. H.; Gonzalez, F. J. Optimization of harvesting, extraction, and analytical protocols for UPLC-ESI-MS-based metabolomic analysis of adherent mammalian cancer cells. *Anal. Bioanal. Chem.* **2013**, *405*, 5279–5289.
- (28) Wu, H.; Southam, A. D.; Hines, A.; Viant, M. R. High-throughput tissue extraction protocol for NMR- and MS-based metabolomics. *Anal. Biochem.* **2008**, *372*, 204–212.
- (29) Savitzky, A.; Golay, M. J. E. Smoothing and differentiation of data by simplified least squares procedures. *Anal. Chem.* **1964**, *36*, 1627–1639.
- (30) Horai, H.; Arita, M.; Kanaya, S.; Nihei, Y.; Ikeda, T.; Suwa, K.; Ojima, Y.; Tanaka, K.; Tanaka, S.; Aoshima, K.; et al. MassBank: a public repository for sharing mass spectral data for life sciences. *J. Mass Spectrom.* **2010**, *45*, 703–714.
- (31) Meierhofer, D.; Weidner, C.; Hartmann, L.; Mayr, J. A.; Han, C.-T.; Schroeder, F. C.; Sauer, S. Protein sets define disease states and predict in vivo effects of drug treatment. *Mol. Cell. Proteomics* **2013**, *12*, 1965–1979.
- (32) Wiśniewski, J. R.; Zougman, A.; Mann, M. Combination of FASP and StageTip-based fractionation allows in-depth analysis of the

- hippocampal membrane proteome. *J. Proteome Res.* **2009**, *8*, 5674–5678.
- (33) Cox, J.; Mann, M. MaxQuant enables high peptide identification rates, individualized p.p.b.-range mass accuracies and proteome-wide protein quantification. *Nat. Biotechnol.* **2008**, *26*, 1367–1372.
- (34) Subramanian, A.; Tamayo, P.; Mootha, V. K.; Mukherjee, S.; Ebert, B. L.; Gillette, M. A.; Paulovich, A.; Pomeroy, S. L.; Golub, T. R.; Lander, E. S.; et al. Gene set enrichment analysis: a knowledge-based approach for interpreting genome-wide expression profiles. *Proc. Natl. Acad. Sci. U.S.A.* **2005**, *102*, 15545–15550.
- (35) Franceschini, A.; Szklarczyk, D.; Frankild, S.; Kuhn, M.; Simonovic, M.; Roth, A.; Lin, J.; Minguez, P.; Bork, P.; von Mering, C.; et al. STRING v9.1: protein–protein interaction networks, with increased coverage and integration. *Nucleic Acids Res.* **2013**, *41*, D808–15.
- (36) Cline, M. S.; Smoot, M.; Cerami, E.; Kuchinsky, A.; Landys, N.; Workman, C.; Christmas, R.; Avila-Campilo, I.; Creech, M.; Gross, B.; et al. Integration of biological networks and gene expression data using Cytoscape. *Nat. Protoc.* **2007**, *2*, 2366–2382.
- (37) Assenov, Y.; Ramírez, F.; Schelhorn, S.-E.; Lengauer, T.; Albrecht, M. Computing topological parameters of biological networks. *Bioinformatics* **2008**, *24*, 282–284.
- (38) Robinson, B. Human complex I deficiency: clinical spectrum and involvement of oxygen free radicals in the pathogenicity of the defect. *Biochim. Biophys. Acta, Bioenerg.* **1998**, *1364*, 271–286.
- (39) Loeffen, J. L.; Smeitink, J. A.; Trijbels, J. M.; Janssen, A. J.; Triepels, R. H.; Sengers, R. C.; van den Heuvel, L. P. Isolated complex I deficiency in children: clinical, biochemical and genetic aspects. *Hum. Mutat.* **2000**, *15*, 123–134.
- (40) Psychogios, N.; Hau, D. D.; Peng, J.; Guo, A. C.; Mandal, R.; Bouatra, S.; Sinelnikov, I.; Krishnamurthy, R.; Eisner, R.; Gautam, B.; et al. The human serum metabolome. *PLoS One* **2011**, *6*, e16957.
- (41) Meierhofer, D.; Mayr, J. A.; Fink, K.; Schmeller, N.; Kofler, B.; Sperl, W. Mitochondrial DNA mutations in renal cell carcinomas revealed no general impact on energy metabolism. *Br. J. Cancer* **2006**, *94*, 268–274.
- (42) Cohadon, F.; Rigoulet, M.; Guérin, B.; Vandendriessche, M. [Vasogenic cerebral oedema. Changes in membrane ATPases. Correction by a phospholipid precursor (author's transl)]. *Nouv. Presse Med.* **1979**, *8*, 1589–1591.
- (43) Yasuda, R.; Noji, H.; Kinoshita, K.; Yoshida, M. F1-ATPase is a highly efficient molecular motor that rotates with discrete 120° steps. *Cell* **1998**, *93*, 1117–1124.
- (44) Smith, C. P.; Thorsness, P. E. Formation of an energized inner membrane in mitochondria with a gamma-deficient F1-ATPase. *Eukaryotic Cell* **2005**, *4*, 2078–2086.
- (45) Wittig, I.; Meyer, B.; Heide, H.; Steger, M.; Bleier, L.; Wumaier, Z.; Karas, M.; Schägger, H. Assembly and oligomerization of human ATP synthase lacking mitochondrial subunits a and A6L. *Biochim. Biophys. Acta* **2010**, *1797*, 1004–1011.
- (46) Capaldo, L.; Montembault, E.; Takeda, T.; Bassi, Z. I.; Glover, D. M.; D'Avino, P. P. The chromosomal passenger complex controls the function of endosomal sorting complex required for transport-III Snf7 proteins during cytokinesis. *Open Biol.* **2012**, *2*, 120070.
- (47) Glotzer, M. The 3Ms of central spindle assembly: microtubules, motors and MAPs. *Nat. Rev. Mol. Cell Biol.* **2009**, *10*, 9–20.
- (48) Hu, C.-K.; Coughlin, M.; Mitchison, T. J. Midbody assembly and its regulation during cytokinesis. *Mol. Biol. Cell* **2012**, *23*, 1024–1034.
- (49) Choi, W.-S.; Kruse, S. E.; Palmiter, R. D.; Xia, Z. Mitochondrial complex I inhibition is not required for dopaminergic neuron death induced by rotenone, MPP+, or paraquat. *Proc. Natl. Acad. Sci. U.S.A.* **2008**, *105*, 15136–15141.
- (50) Allani, P. K.; Sum, T.; Bhansali, S. G.; Mukherjee, S. K.; Sonee, M. A comparative study of the effect of oxidative stress on the cytoskeleton in human cortical neurons. *Toxicol. Appl. Pharmacol.* **2004**, *196*, 29–36.
- (51) Currais, A.; Hortobágyi, T.; Soriano, S. The neuronal cell cycle as a mechanism of pathogenesis in Alzheimer's disease. *Aging* **2009**, *1*, 363–371.
- (52) Chen, H.; Chomyn, A.; Chan, D. C. Disruption of fusion results in mitochondrial heterogeneity and dysfunction. *J. Biol. Chem.* **2005**, *280*, 26185–26192.
- (53) Hower, V.; Mendes, P.; Torti, F. M.; Laubenbacher, R.; Akman, S.; Shulaev, V.; Torti, S. V. A general map of iron metabolism and tissue-specific subnetworks. *Mol. BioSyst.* **2009**, *5*, 422–443.
- (54) Mena, N. P.; Bulteau, A. L.; Salazar, J.; Hirsch, E. C.; Núñez, M. T. Effect of mitochondrial complex I inhibition on Fe–S cluster protein activity. *Biochem. Biophys. Res. Commun.* **2011**, *409*, 241–246.
- (55) Saito, Y. Oxidized DJ-1 as a possible biomarker of Parkinson's disease. *J. Clin. Biochem. Nutr.* **2014**, *54*, 138–144.
- (56) Lev, N.; Ickowicz, D.; Melamed, E.; Offen, D. Oxidative insults induce DJ-1 upregulation and redistribution: implications for neuroprotection. *Neurotoxicology* **2008**, *29*, 397–405.
- (57) Valsecchi, F.; Grette, S.; Roestenberg, P.; Joosten-Wagenaars, J.; Smeitink, J. A. M.; Willems, P. H. G. M.; Koopman, W. J. H. Primary fibroblasts of NDUFS4^{-/-} mice display increased ROS levels and aberrant mitochondrial morphology. *Mitochondrion* **2013**, *13*, 436–443.